Steel and Composite Structures, *Vol. 28, No. 5 (2018) 641-653*
DOI: https://doi.org/10.12989/scs.2018.28.5.641

Experiment and bearing capacity analyses of dual-lintel column joints in Chinese traditional style buildings

Jianyang Xue [a], Linlin Ma [*], Zhanjing Wu [b], Lei Zhai [c] and Xin Zhang [d]

College of Civil Engineering, Xi'an University of Architecture and Technology, Xi'an 710055, China

(*Received April 18, 2018, Revised June 11, 2018, Accepted June 17, 2018*)

Abstract. This paper presents experiment and bearing capacity analyses of steel dual-lintel column (SDC) joints in Chinese traditional style buildings. Two SDC interior joints and two SDC exterior joints, which consisted of dual box-section lintels, circular column and square column, were designed and tested under low cyclic loading. The force transferring mechanisms at the panel zone of SDC joints were proposed. And also, the load-strain curves at the panel zone, failure modes, hysteretic loops and skeleton curves of the joints were analyzed. It is shown that the typical failure modes of the joints are shear buckling at bottom panel zone, bending failure at middle panel zone, welds fracturing at the panel zone, and tension failure of base metal in the heat-affected zone of the joints. The ultimate bearing capacity of SDC joints appears to decrease with the increment of axial compression ratio. However, the bearing capacities of exterior joints are lower than those of interior joints at the same axial compression ratio. In order to predict the formulas of the bending capacity at the middle panel zone and the shear capacity at the bottom panel zone, the calculation model and the stress state of the element at the panel zone of SDC joints were studied. As the calculated values showed good agreements with the test results, the proposed formulas can be reliably applied to the analysis and design of SDC joints in Chinese traditional style buildings.

Keywords: Chinese traditional style building; low cyclic loading; bending capacity; shear bearing capacity; steel dual-lintel column joints

1. Introduction

China has a long-standing glorious and brilliant historical culture, especially Chinese ancient architecture, which differs greatly from western traditional buildings in many aspects: material, structural system, space layout, and cultural values (Zhang *et al.* 2011). Chinese ancient architecture reflects distinctive national characteristics, and has a high value in terms of history, culture, art and science. The earliest Chinese timber architecture that has ever been found is more than 5,000 years ago. The first book on the construction of timber structures (Li 1100) was published in the Song Dynasty (A.D. 960-1279), and the studies about timber structures start at the 1970s (Liang 1984). As times goes on, the well preserved Chinese timber buildings have been scarce through a variety of natural disasters and wars so far. And also, wood structures are vulnerable to fire, and are difficult to be used for large and complex buildings (Xue and Qi 2016).

To inherit and promote the traditional culture, Chinese traditional style buildings constructed with modern construction materials emerge in many ancient cities. As the carriers of ancient culture and modern technologies, Chinese traditional style buildings spread Chinese ancient culture and embody the essence of Chinese ancient architecture. Steel has been widely adopted in Chinese traditional style buildings because of its better properties, such as high-strength and light-weight, better seismic performance and recyclability.

Fig. 1 shows a type of special joints (dual-lintel column joints) in Chinese traditional style buildings, which consists of dual lintels and singular column. To meet the appearance of Chinese ancient buildings, the column is erected as a circular cross-section and the box section is applied to the lintels.

The beam-column joints transferring the shear force and bending moment is the key component of steel frame (Chen and Lin 2013, Loulelis *et al.* 2012, Gholami *et al.* 2013 and Lee *et al.* 2013). Many researchers studied seismic performance of steel beam-column joints by experimental and numerical analyses. Kim and Hwang (2008) investigated the strength behaviors of the joints of steel box-beams and circular columns. Wang *et al.* (2011) investigated seismic performance of steel beam to circular tubular column joints with outer diaphragm. Test results indicated that shearing buckling and local distortion of outer diaphragm occurred at the joints, and weak panel connections demonstrated better seismic performance and ductility. Hiroki *et al.* (2011) performed the loading tests on beam-column joints with exterior diaphragm and circular tube column. Shi *et al.* (2012) performed monotonic loading tests on semi-rigid end-plate connections with welded I-

*Corresponding author, Ph.D. Candidate, E-mail: linling_ma@163.com
[a] Ph.D., Professor, E-mail: jianyang_xue@163.com
[b] Ph.D., E-mail: zhanjing_wu@163.com
[c] Ph.D. Candidate, E-mail: leizhai_chn@163.com
[d] Ph.D. Candidate, E-mail: civil_xinzhang@163.com

ISSN: 1229-9367 (Print), 1598-6233 (Online)

(a) Chinese traditional style buildings

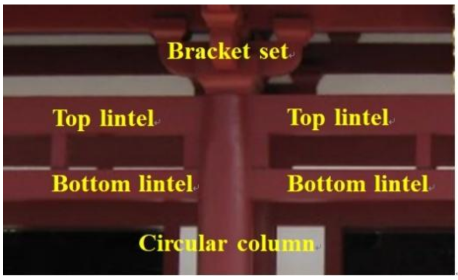

(b) Sketch of SDC joints

Fig. 1 Dual-lintel column joints of Chinese traditional style buildings

shaped columns and beams. The different measurement methods on beam-to-column joint rotation in steel frames were compared. Lan and Huang (2016) presented a numerical parametric study on ultimate strength of cold-formed stainless steel tubular X- and T-joints at elevated temperatures. Kim *et al*. (2016) studied the influence of steel joints upon the flexural capacity of precast concrete columns, and predicted the flexural moment capacity of concrete columns with hybrid composite joints. Moradi and Alam (2017) used a response surface methodology to predict and optimize the lateral response characteristics of posttensioned steel beam-column joints with top-and-seat angles.

To archaize the appearance of Chinese ancient buildings, Chinese traditional style buildings was built by modern materials and construction process according to the construction rules of Chinese ancient buildings. Therefore, the seismic performance of Chinese traditional style buildings was different from those of the Chinese ancient timber structures with mortise-tenon joints and conventional modern buildings (D'Ayala and Benzoni 2012). However, the researches on Chinese traditional style buildings are rather few at present (Xue and Qi 2016). As a symbol of Chinese traditional style buildings, dual-lintel column joints play a decorative role in the appearance of the buildings and change the force transfer mechanisms of the buildings. The panel zone of SDC joints are divided into top panel zone (the connection among top lintels, circular column and square column), middle panel zone (the part between top lintels and bottom lintels), and bottom panel zone (the connection between bottom lintels and circular column), as shown in Fig. 2. Common beam-column joints only have one panel zone, so the mechanical properties and deformation characteristics of the joints are significantly different from the common joints. Therefore, it is necessary to carry out research on force transfer mechanisms and seismic behavior of the joints both experimentally and theoretically.

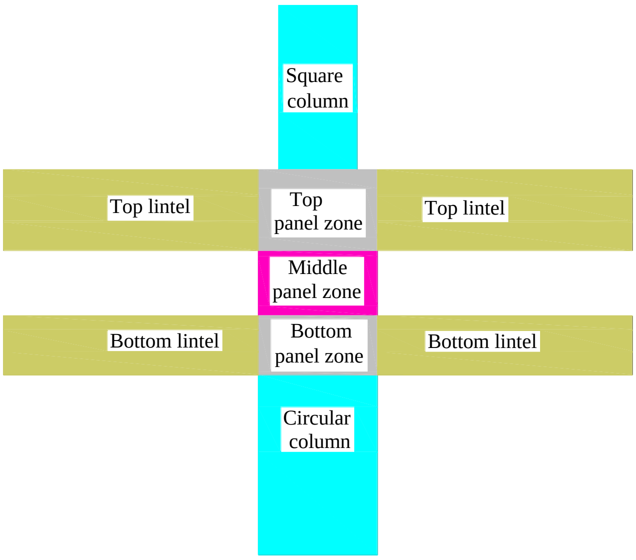

Fig. 2 Sketch of the panel zone of specimens

In order to provide theoretical guidance for the application of Chinese traditional style buildings, four 1/2-scaled SDC joints were designed and conducted under low cyclic loading. The force mechanisms and failure modes, hysteretic loops and skeleton curves of the joints with different connection configuration and axial compression ratio were analyzed. Formulas for shear capacity of the bottom panel zone were also derived. As the calculated values showed good agreements with the test results, the proposed formulas can be applied to the analysis and design of SDC joints in Chinese traditional style buildings.

2. Experimental program

2.1 Specimen design and construction

To study the influence of axial compression ratio and joint configuration on seismic performance of SDC joints in Chinese traditional style buildings, four SDC joints were designed and conducted under low cyclic loading. The specimens including exterior joints (EJ) series and interior joints (IJ) series with different joint configuration, were designated as EJ - 1, EJ - 2 and IJ - 1, IJ - 2 with different axial compression ratio 0.3 and 0.6 for each series, respectively. The prototype of this test was extracted from a palace style building in Mount Putuo Buddhist Academy built at Zhoushan Islands on east coast of China. Referring to the palace style buildings and combining the dimension of Chinese ancient buildings, the prototype size was finally converted and determined by the length unit in Construction Methods of Song dynasty (Li 1100), and the scaled of the specimens was 1:2.

Keeping the main characteristics of Chinese traditional style buildings, the specimens were selected from the part among the infection points of lintels and column under lateral loading. And also, the overall length of square

Table 1 Design parameters of specimens

Specimen No.	Top lintel		Bottom lintel		Circular column		Square column (mm)	Axial compression ratio
	Flange (mm)	Web (mm)	Flange (mm)	Web (mm)	Other area (mm)	Panel zone (mm)		
IJ1	260×20	170×16	230×20	155×16	Φ356×16	Φ356×6	□210×16	0.3
IJ2	260×20	170×16	230×20	155×16	Φ356×16	Φ356×6	□210×16	0.6
EJ1	260×20	170×16	230×20	155×16	Φ356×16	Φ356×6	□210×16	0.3
EJ2	260×20	170×16	230×20	155×16	Φ356×16	Φ356×6	□210×16	0.6

column and circular column is 2250 mm, and the distance between the centre of the joints and the outer ends of lintels is 1248 mm. The designed parameters of the joints are listed in Table 1.

To study the seismic performance and bearing capacity at the panel zone of SDC joints, the specimens were designed by the principle of "strong members-weak joints", which assured that the failure of the panel zone was earlier than the appearance of plastic hinges of lintel-ends and column-ends. Therefore, the circular column was comprised of two seamless steel tubes, including a 6 mm thick tube in the panel zone and a 16 mm thick tube out of the panel zone. The panel zone was divided into three parts—top panel zone, middle panel zone and bottom panel zone, as shown in Fig. 2.

To ensure the accuracy of specimens, all specimens were made in professional fabricating plant. And also, the specimens were constructed by the welding procedures and detailing requirements in Code for Design of Steel Structures (GB50017-2003) and Code for Welding of Steel Structures (GB50661-2011). The manufacturing process of specimens was as follows: welding of square column and lintels, making of the panel zone, combining of circular column, and connecting of lintels and columns.

Dimensions and details of the specimens are shown in Fig. 3. Circular column was made of two seamless steel tubes, and square column and lintels were welded by four hot-rolled steel plates. To transfer the forces from the top of the square column to the circular column, the square column was inserted into the circular column to the corresponding level of the top lintel-bottom flange and connected by four vertical diaphragms. And also, four lateral diaphragms were weld in the circular column to restrict the deformation of the panel zone. The connections

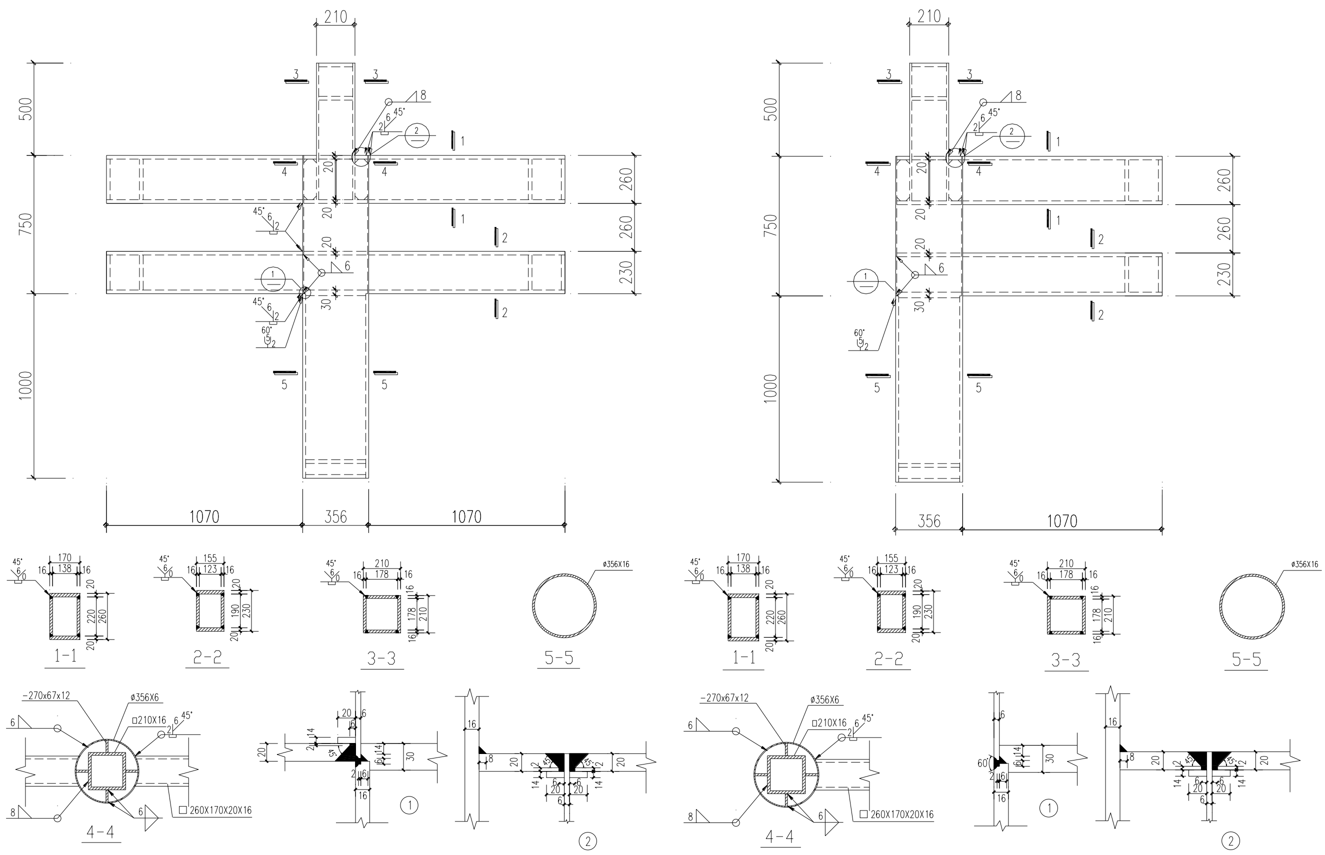

(a) Interior joints (IJ-1, IJ-2)

(b) Exterior joints (EJ-1, EJ-2)

Fig. 3 Details of specimens

Table 2 Mechanic performance indexes

Material	Plate thickness t (mm)	Yield stress f_y (MPa)	Tensile strength f_u (MPa)	Elastic modulus E (MPa)	Yield strain ε_y
Steel plates	12	318.9	472.3	2.077×10^5	1535×10^{-6}
	16	289.7	436.7	2.106×10^5	1375×10^{-6}
	20	268.9	406.6	2.130×10^5	1262×10^{-6}
Steel tubes	6	323.0	425.6	2.101×10^5	1537×10^{-6}
	16	301.7	438.9	2.121×10^5	1472×10^{-6}

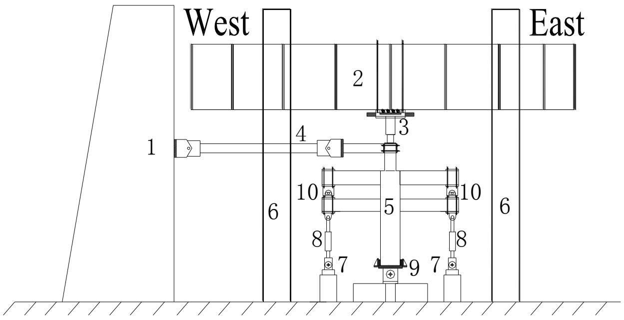

1. Reaction wall 2. Reaction girder 3. Vertical actuator
4. Horizontal actuator 5. Specimen 6. Reaction steel frame
7. Single-hinge support at lintel end 8. Load cell
9. Single-hinge support under column
10. Connector of dual lintels

Fig. 4 Test setup

between all components were full penetration groove welding according to Chinese Code for Welding of Steel Structures (GB50661-2011). All specimens were made of Q235 steel, and the material properties of specimens are shown in Table 2.

2.2 Test setup and procedure

The basic configuration of a typical test setup and the location of instrumentations are represented in Fig. 4. The specimens were pinned at the bottom end of circular column and bottom lintel ends and free at the top end of square column to simulate the conditions of SDC joints under the action of earthquake. The axial compression load was applied to square column by a vertical jack with a 1,000 kN capacity in compression and kept constant during the test process. Then lateral load was applied to the top end of square column by horizontal actuator, which had a force capacity of ± 1,000 kN and a displacement capacity of ± 350 mm. The vertical jack can move as the specimens deformed during the test.

A typical dual-lintel connector was designed between the top lintel and bottom lintel in Fig. 5. The top slotted-plate and bottom slotted-plate were respectively connected with the top lintel and bottom lintel by high-strength bolts. In order to have a relative movement in the horizontal direction and keep the vertical distance constant between top lintel and bottom lintel, a roller was installed in slotted holes between the top slotted-plate and bottom slotted-plate. Therefore, the dual-lintel connector cannot transfer the shear force and bending moment from top lintel, and there was only vertical force between the top lintel-ends and bottom lintel-ends.

According to Chinese Code for Specification for Seismic Test of Buildings (JGJ/T101-2015), the loading history included a load-controlled step and a displacement-controlled step, as illustrated in Fig. 6. At the initial phase, the tests were in load-controlled stage, in which the horizontal loads linearly changed with an interval of 10 kN, and every load step was circulated one cycle. After specimens started yielding, the tests were conducted under displacement control. Each displacement-loading level was applied three cycles with the increment of 10 mm until the load dropped below 85% of the peak loading.

Displacement transducers were installed at the lintel-

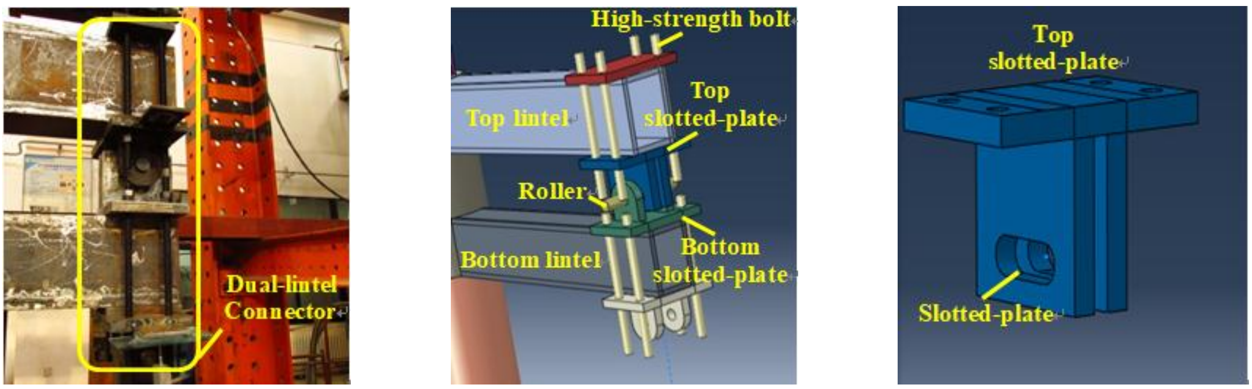

(a) Connector between dual lintels (b) Details of dual-lintel connector (c) Top slotted-plate

Fig. 5 Connector between top lintels and bottom lintels

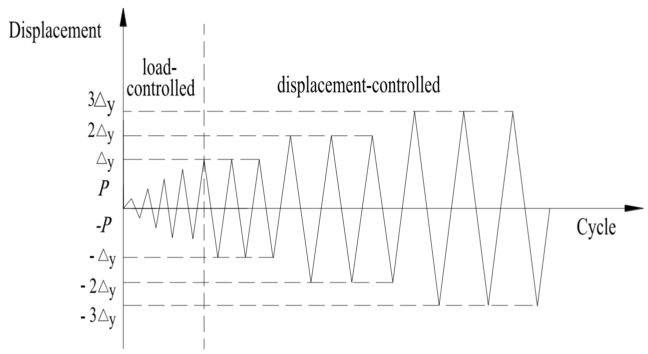

Fig. 6 Loading history

ends and along the height of circular column to measure the displacements of specimens. The load of lintel-ends was measured by two load cell installed at the bottom lintel-ends. Strain gages were set to capture strains adjacent to the panel zone, the webs and flanges of columns, and the webs and flanges of lintels. In addition, six strain gages were diagonally mounted to measure the shear deformation of specimens. The arrangement of measuring points is shown in Fig. 7.

3. Experimental results

3.1 Failure procedure

Four specimens have the similar failure process. The failure of specimens began at the panel zone because of the designed-principle of strong-member and weak-panel zone. It can be determined from the values measured by strain gages that the diagonal part of the bottom panel zone yielded first, and then the middle panel zone began to yield from the webs of the circular column. The tendency of strains at the panel zone of EJ-1 is shown in Fig. 8, in which P is the load at the top end of the square column, and ε is the strains measured by strain gages.

After the panel zone yielding, there were four types of failure patterns occurring in sequence during the following loading process:

(1) Typical shear buckling formed at the bottom panel zone (Fig. 9(a)), which is resulted from the fact that the panel zone was designed by the principle of strong-member and weak-panel zone. In addition, two lateral diaphragms and four vertical diaphragms

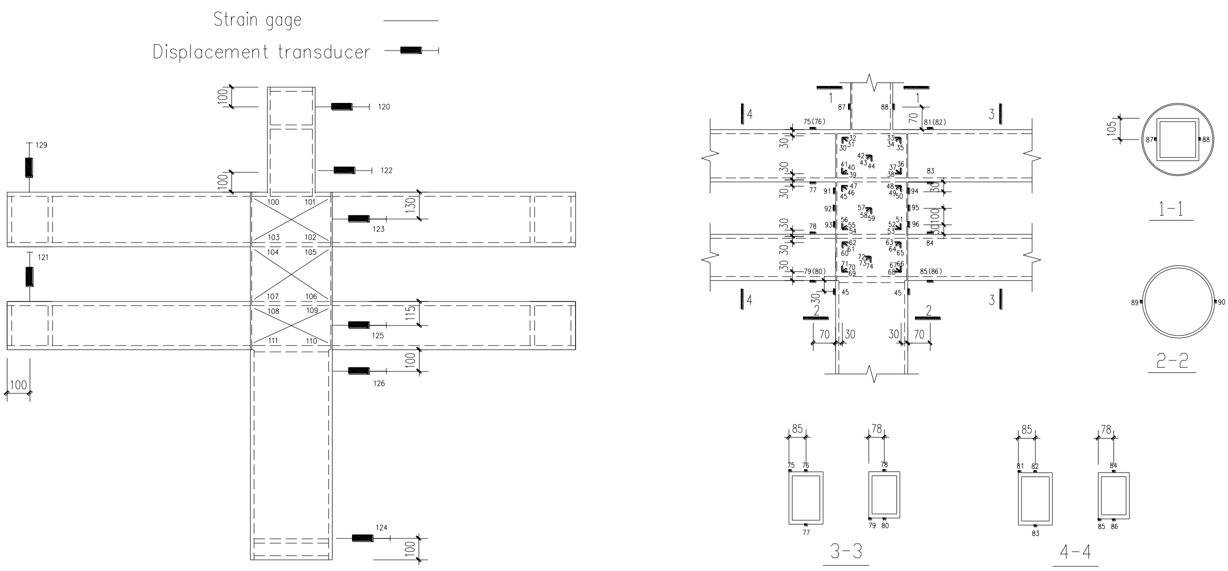

(a) South of specimen

(b) North of specimen

Fig. 7 Measuring points of specimens

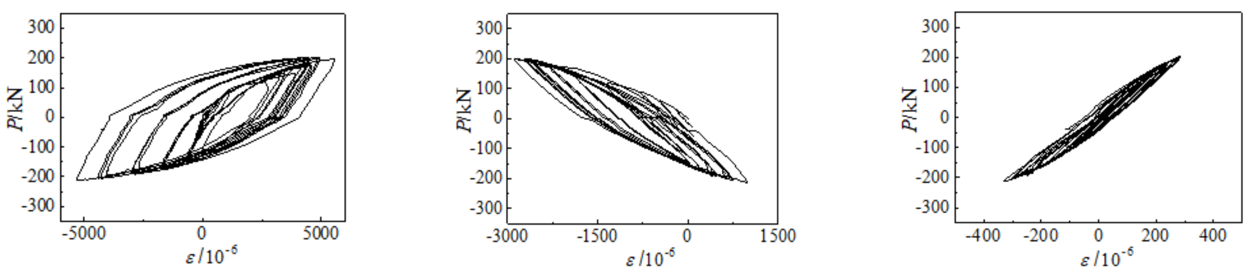

(a) Strain at the bottom panel zone (Strain gage 67 of EJ-1)

(b) Strain at the middle panel zone (Strain gage 46 of EJ-1)

(c) Strain at the top panel zone (Strain gage 37 of EJ-1)

Fig. 8 Strain of the panel zone

were welded in the circular column at the top panel zone, and the internal force of bottom panel zone was larger than that of the middle panel zone, so buckling started at the bottom panel zone.

(2) Welds fracturing occurred at the connections between the bottom flanges of bottom lintels and circular column-flanges (Fig. 9(b)) for IJ series as well as the connections between the top flanges of top lintels and circular column-flanges (Fig. 9(c)) for EJ series. Then the fractures developed to the adjacent webs of circular column or lintels. The reason was that there was serious stress concentration at the toe of welds at the fracturing connections, and the shearing force and bending moment of the sections at the fracturing connections are the largest among the components of specimens.

(3) Bending buckling occurred at the flanges of circular column at the middle panel zone (Fig. 9(a)) for IJ-2 and EJ-2, which had a larger axial compression ratio 0.6. The reason was that the *P*-*Δ* effect caused by the axial force of square column was enough significant for IJ-2 and EJ-2 to bend the flanges of circular column at the middle panel zone with the increment horizontal displacement.

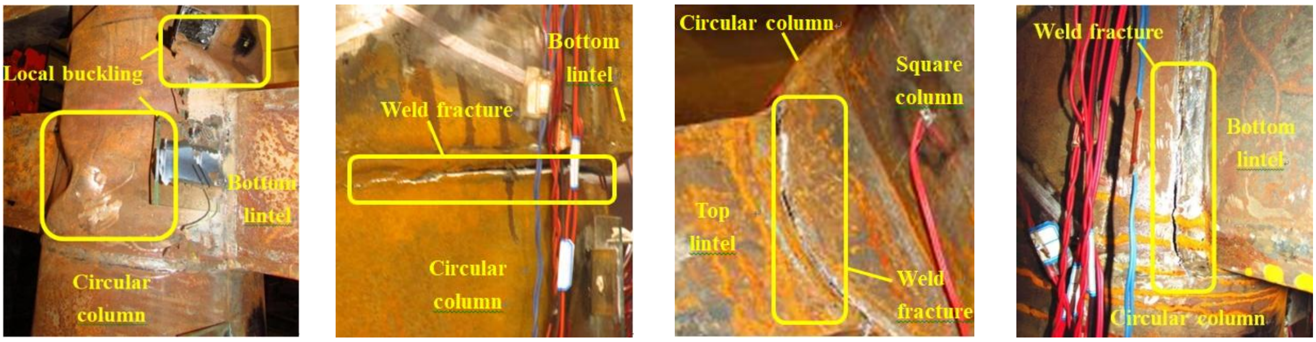

(a) Local buckling (IJ-2) at the panel zone

(b) Welds fracturing (IJ-1) at the bottom panel zone

(c) Welds fracturing (EJ-1) at the top panel zone

(d) Welds fracturing (EJ-2) at the bottom panel zone

Fig. 9 Failure modes of specimens

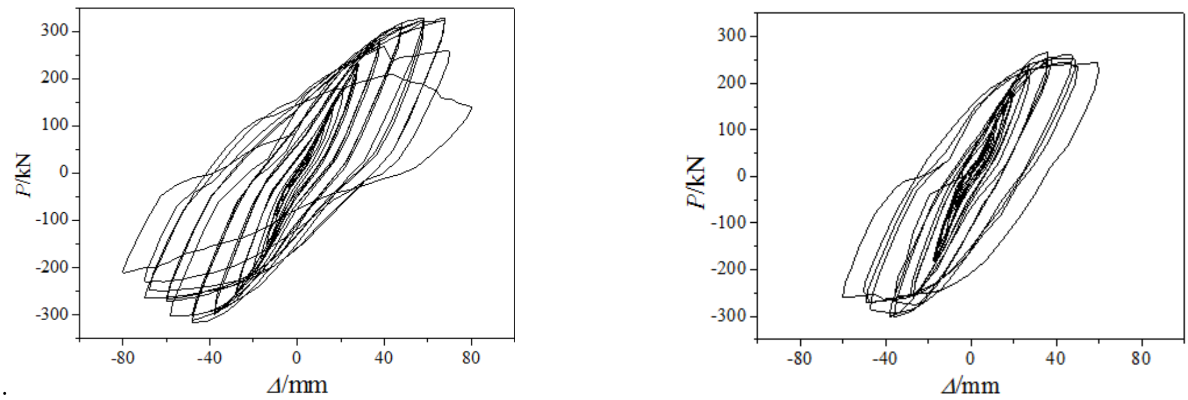

(a) IJ-1

(b) IJ-2

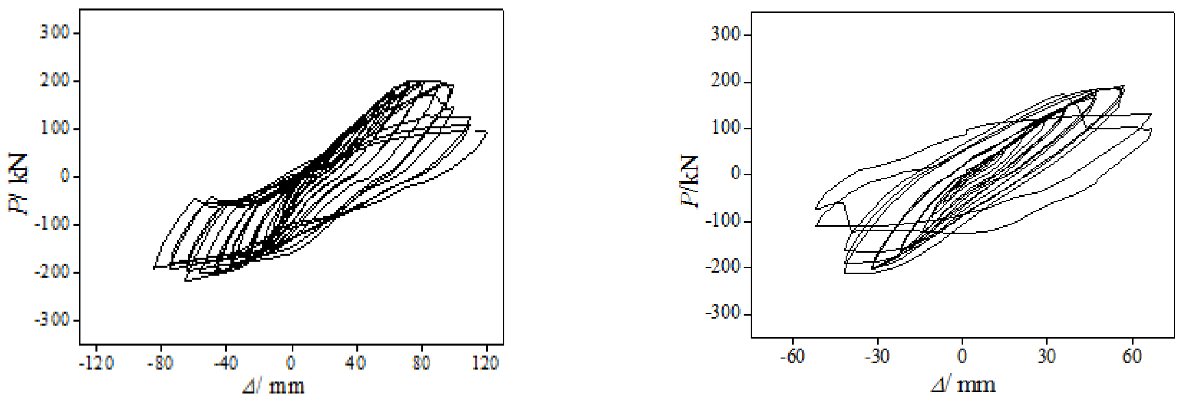

(c) EJ-1

(d) EJ-2

Fig. 10 *P*-Δ hysteretic loops of specimens

(4) For EJ series, welds between the bottom flanges of bottom lintels and circular column-flanges cracked (Fig. 9(d)), and then the cracks developed finally to the adjacent webs of lintels. It was resulted from that the mechanical modes of EJ series was similar to the common joints with single lintel and column after welds fracturing occurred at the connections between the top flanges of top lintels and circular column-flanges. Therefore, the connections between the bottom flanges of bottom lintels and circular column-flanges had the maximum section internal force, which resulted in the welds cracking.

Until the loading ended, no yield occurred at the top panel zone and ends of lintels and columns, as shown in Fig. 9.

3.2 Hysteretic loops

The *P*-Δ hysteretic loops are shown in Fig. 10, in which *P* and Δ is the load and displacement at the top end of square column, respectively. It is shown that the hysteretic loops are full, which are in shuttle shape, indicating that SDC joints have better hysteretic performance. And also, the hysteretic loops of IJ series are fuller than those of EJ series. The reason was that the restrain effect of four lintels on the panel zone of IJ series is larger than that of two lintels on the panel zone of EJ series, so it takes more force for IJ series to reach the same deformation.

The skeleton curves are shown in Fig. 11. Three critical characteristic points of specimens, namely, yield point, ultimate point and failure point can be obtained from the skeleton curves, in which the yield point can be defined by the Uniform Yield Moment Method, and the failure point corresponds to the point when the load of specimen drops to 85% of the maximum load with the increase of deformation. The loads and displacements corresponding to these three points of specimens are listed in Table 3. And also, the yield values of bottom panel zone are obtained. From Fig. 11 and Table 3, it can be found that the bearing capacity of IJ-1 (or IJ-2) are much higher than that of EJ-1 (or EJ-2), which indicates that configurations of SDC joints have a significant impact on the bearing capacities of the joints. In addition, IJ-1 (or EJ-1) has a larger bearing capacity than IJ-2 (or EJ-2), showing that when the axial compression ratio is less than 0.6, it has a significant effect on the bearing capacity of SDC joints. The reason was that after welds between lintels and circular column cracked, the *P*-Δ effect caused by the axial force of square column was too significant to bend the flanges of the circular column at the middle panel zone for IJ-2 and EJ-2 with the increment of horizontal displacement. So the bearing capacities of IJ-2 and EJ-2 with a larger axial compression ratio 0.6 decreased.

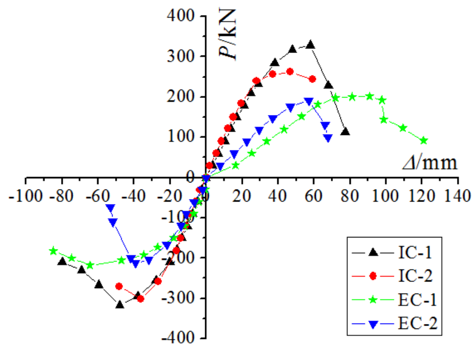

Fig. 11 Skeleton curves of specimens

According to the test phenomena and analyses of test results, the failure modes of SDC joints were mainly shearing failure at the bottom panel zone and local buckling on both sides of the middle panel zone. Therefore, in order to assure that the SDC joints have enough bearing capacity, it is necessary to predict the shear capacity at the bottom panel zone and check the bending capacity at the middle panel zone.

4. Calculation of shear capacity at the bottom panel zone

Table 3 Summary of measured resultstt

Specimen No.	Loading direction	Dual-lintel column joints						Bottom panel zone	
		P_y/kN	Δ_y/mm	P_u/kN	Δ_u/mm	P_m/kN	Δ_m/mm	P_s/kN	Δ_s/mm
IJ-1	Positive	233.02	26.97	328.56	56.95	279.28	69.49	138.96	17.64
	Negative	-256.77	-27.33	-316.85	-47.00	-269.32	-60.06		
IJ-2	Positive	232.44	26.82	261.54	47.92	222.31	67.96	113.22	13.78
	Negative	-217.63	-22.13	-301.64	-37.92	-257.43	-58.03		
EJ-1	Positive	159.82	59.97	201.07	96.93	170.91	100.68	137.96	55.78
	Negative	-153.70	-24.97	-217.84	-64.54	-185.16	-74.16		
EJ-2	Positive	161.39	38.96	191.11	53.99	162.44	57.33	117.11	31.07
	Negative	-177.42	-25.00	-212.79	-42.23	-212.79	-42.23		

*Note: The pushed direction of horizontal actuator is defined as positive, and the pulled direction is defined as negative. P_y and P_u stand for the yield load and the ultimate load of the joints, respectively; P_m corresponds to the load of 0.85 P_u. Δ_y, Δ_u, and Δ_m are the displacements corresponding to P_y, P_u, and P_m. P_s stands for the load when the diagonal strain of bottom panel zone reaches the yield strain of steel, and Δ_s is the displacement corresponding to P_s

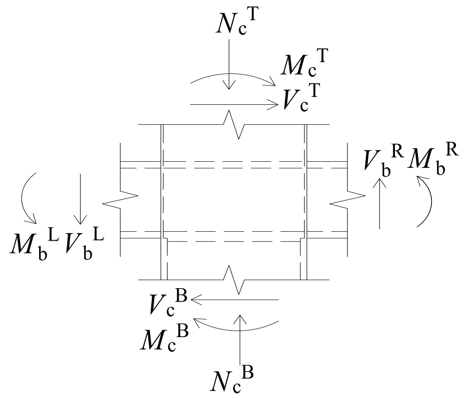

(a) The force model of bottom panel zone

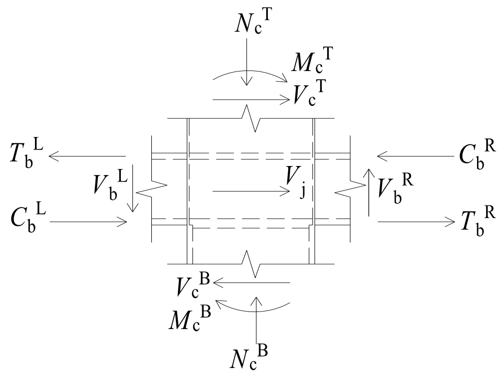

(b) The shear analysis model of bottom panel zone

Fig. 12 Calculation model of shearing force at bottom panel zone for IJ series

4.1 Calculation of lateral shear

Taking IJ series as an example, bottom panel zone is fetched as partition. The internal forces of bottom panel zone are shown in Fig. 12. From equilibrium conditions of the partition, we can obtain the two following equations

$$M_b^L + M_b^R = M_c^T + M_c^B \tag{1}$$

$$V_j = T_b^R + C_b^L - V_c^B \tag{2}$$

where $M_b{}^L$ = bending moment of left bottom lintel-end near bottom panel zone; $M_b{}^R$ = bending moment of right bottom lintel-end near bottom panel zone; $M_c{}^T$ = bending moment of circular column-end at middle panel zone; $M_c{}^B$ = bending moment of circular column-end near bottom panel zone; V_j = shearing force at bottom panel zone; $T_b{}^R$ = equivalent tensile force at right bottom lintel-end near bottom panel zone; $C_b{}^L$ = equivalent compressive force at left bottom lintel-end near bottom panel zone; $V_c{}^B$ = shearing force of circular column-end near bottom panel zone; $N_c{}^T$ = axial force of circular column-end at middle panel zone; $N_c{}^B$ = axial force of circular column-end near bottom panel zone; $V_c{}^T$ = shearing force of circular column-end at middle panel zone; $V_b{}^L$ = shearing force of left bottom lintel-end near bottom panel zone; $V_b{}^R$ = shearing force of right bottom lintel-end near bottom panel zone; $T_b{}^L$ = equivalent tensile force at left bottom lintel-end near bottom panel zone; $C_b{}^R$ = equivalent compressive force at right bottom lintel-end near bottom panel zone.

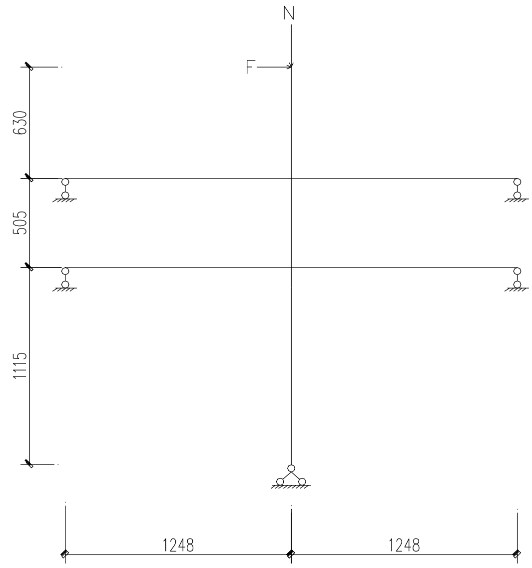

(a) Simplified model of internal force for IJ series

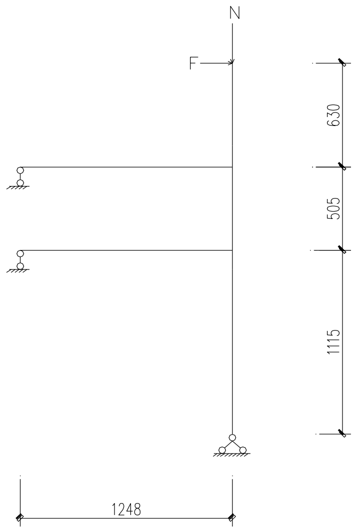

(b) Simplified model of internal force for EJ series

Fig. 13 Calculation model of SDC joints

For IJ series, $T_b{}^L$, $C_b{}^L$, $T_b{}^R$ and $C_b{}^R$ are compressive shearing force calculated by $M_b{}^L$ and $M_b{}^R$. Assuming that h_{bw} is the distance between the centroids of bottom lintel flanges, two different equations are obtained as follows

$$T_b^R = C_b^R = \frac{M_b^R}{h_{bw}}, \qquad T_b^L = C_b^L = \frac{M_b^L}{h_{bw}} \tag{3}$$

In the case of EJ series, a similar procedure can be used, and the following equations are obtained

$$M_b = M_c^T + M_c^B \tag{4}$$

$$V_j = C_b - V_c^B \tag{5}$$

where M_b = bending moment of bottom lintel-end near

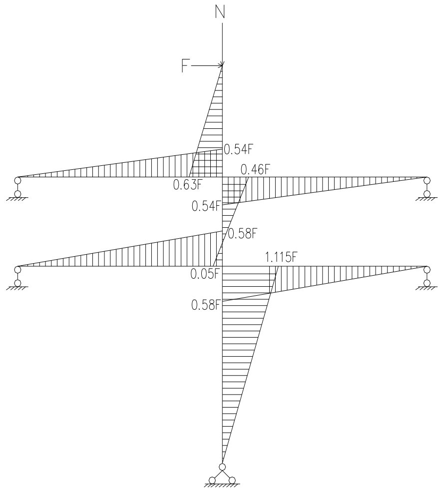

(a) Bending moment diagram of IJ series

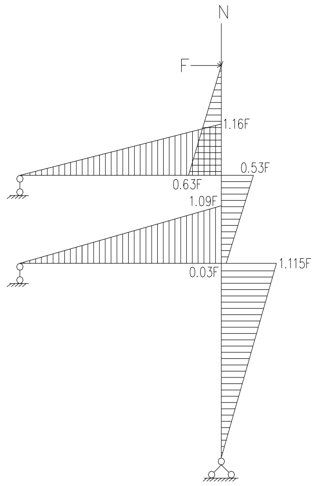

(b) Bending moment diagram of EJ series

Fig. 14 Bending moment diagrams of SDC joints

bottom panel zone. T_b and C_b are compressive shearing force calculated by M_b. Assuming that h_{bw} is the distance between the centroids of bottom lintel flanges, the following equation can be obtained

$$T_b = C_b = \frac{M_b}{h_{bw}} \tag{6}$$

The calculation model of internal force shown in Fig. 13 is adopted to predict the shear capacity of the bottom panel zone, where the bar models are approximated by the neutral axes of each section. And also, the bending moment diagram of the models under axial force N and horizontal force F is shown in Fig. 14 by using the force method in structural mechanics. It indicates that the bottom panel zone is the critical section, so it should be the object to predict the shear capacity of dual-lintel column joints.

The shearing force diagrams of the joints can be gotten by the bending moment diagrams. And then the yield shearing force V_t at the bottom panel zone of IJ series (EJ series) in the test are obtained by putting the values of yield load (P_S), shearing force (V_c^B) and bending moment (M_b^L

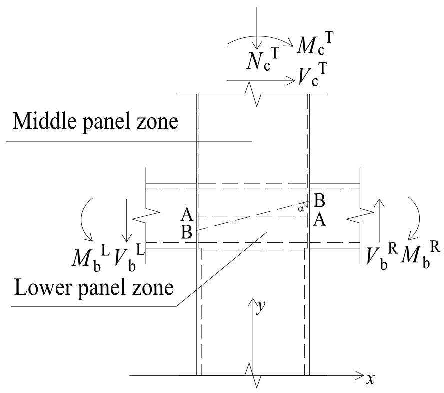

(a) The facade of bottom panel zone

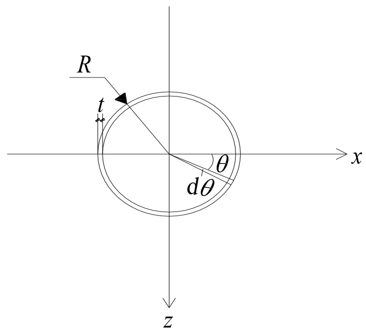

(b) Cross-section dimensions of circular column

Fig. 15 Calculation model at bottom panel zone for IJ series

and M_b^R) into Eqs. (2)-(3) (Eqs. (5)-(6)), as shown in Table 4.

4.2 Connection force model

To investigate the shearing capacity at the bottom panel zone of SDC joints, two sections of circular column are taken into consideration in Fig. 15, namely cross section A-A and inclined section B-B at the bottom panel zone. Assuming that the element at the angle θ on the inclined section B-B is obtained by anticlockwise rotation angle β of the element at the angle θ on section A-A. In Fig. 15, N_c^T is axial force of circular column-end at middle panel zone; V_c^T is shearing force of circular column-end at middle panel zone; M_c^T is bending moment of circular column-end at middle panel zone; M_b^L is bending moment of left bottom lintel-end near bottom panel zone; M_b^R is bending moment of right bottom lintel-end near bottom panel zone; V_b^L is shearing force of left bottom lintel-end near bottom panel zone; V_b^R is shearing force of right bottom lintel-end near bottom panel zone.

From mechanics of materials, shearing stress of random point on circular section is tangent to the circular section, and the maximum shear stress is at the neutral axis of circular column, so its direction is parallel to the shearing force of circular column. At the bottom panel zone of the joints, the normal stress σ_α and shearing stress τ_α of the element at the angle θ on section B-B at the bottom panel zone are given as follows

$$\sigma_\alpha = \frac{\sigma_x + \sigma_y}{2} + \frac{\sigma_x - \sigma_y}{2}\cos 2\alpha - \tau_{xy}\sin 2\alpha \tag{7}$$

$$\tau_\alpha = \frac{\sigma_x - \sigma_y}{2}\sin 2\alpha + \tau_{xy}\cos 2\alpha \tag{8}$$

where σ_x = circumferential tensile stress on section A-A (assuming that σ_x is homogeneous distribution on section A-A); σ_y = vertical normal stress on section A-A under axial force and bending moment, and τ_{xy} = shear stress on section A-A.

The shearing force $V_{B\text{-}B}$ on section B-B is obtained by taking the integral of Eq. (8).

$$\begin{aligned} V_{B\text{-}B} &= \int_A \tau_\alpha \mathrm{d}A \\ &= 2\int_0^\pi \left(\frac{\sigma_x - \sigma_y}{2}\sin 2\alpha - \tau\cos 2\alpha\right)\frac{t}{\sin\alpha}R\mathrm{d}\theta \\ &\approx \pi Rt\cot\alpha\cdot\sigma_x + 2Rt\int_0^\pi \tau_\theta \sin\theta\mathrm{d}\theta \\ &= \frac{A_s}{2}\sigma_x\cot\alpha + \pi Rt\tau_{max} \end{aligned} \tag{9}$$

where A_s = cross-section area of section A-A, τ_{max} = the maximum shearing stress on section A-A.

4.3 The maximum shearing stress

The plane stress state of the element at random angle θ on section B-B is shown in Fig. 16, and the following Eq. (10) is given by the energy intensity theory as follows

$$\sigma_x^2 + \sigma_y^2 - \sigma_x\sigma_y + 3\tau_{xy}^2 = f_y^2 \tag{10}$$

where f_y = yield stress of steel tube in 6 mm thickness.

From mechanics of materials, Eq. (11) is given as follows

$$\sigma_y = -\left(\sigma_y^N + \sigma_y^M\cos\theta\right), \quad \tau_{xy} = -\tau_\theta = -\tau_{max}\sin\theta \tag{11}$$

where σ_y^N = the vertical normal stress generated by axial force N_y^T, σ_y^M = the vertical normal stress generated by bending moment M_c^T and τ_θ = shear stress at angle θ on section B-B.

Introducing Eq. (11) into Eq. (10), we have

$$\begin{aligned} f_y^2 &= \sigma_x^2 + (\sigma_y^N + \sigma_y^M\cos\theta)^2 \\ &+ \sigma_x(\sigma_y^N + \sigma_y^M\cos\theta) + 3\tau_{max}^2\sin^2\theta \end{aligned} \tag{12}$$

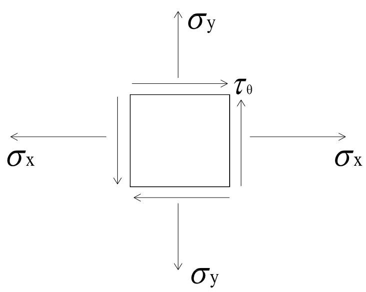

Fig. 16 The stress state of the element on section B-B

Differentiating Eq. (12) gives a different equation of f_y and θ as follows

$$\begin{aligned} 2f_y f_y' &= 6\tau_{max}^2\sin\theta\cos\theta - 2\sigma_y^N\sigma_y^M\sin\theta \\ &- 2(\sigma_y^M)^2\sin\theta\cos\theta - \sigma_x\sigma_y^M\sin\theta \end{aligned} \tag{13}$$

Designating $f'_y = 0$, and Eq. (14) is obtained as follows

$$\cos\theta_0 = \frac{\sigma_y^M(2\sigma_y^N + \sigma_x)}{6\tau_{max}^2 - 2(\sigma_y^M)^2} \tag{14}$$

From Eq. (14), we have

$$\tau_{max} = \sqrt{\frac{f_y^2 - \sigma_x^2 - (\sigma_y^N + \sigma_y^M\cos\theta_0)^2 - \sigma_x(\sigma_y^N + \sigma_y^M\cos\theta_0)}{3\sin^2\theta_0}} \tag{15}$$

where θ_0 = the angle between the most dangerous point and x axis, and τ_{max}= the maximum shear stress on section A-A.

Assuming that the cross-section of circular column meets the assumption of plane-section, and the following equations are obtained as follows

$$\begin{aligned} &\frac{\sigma_s}{E_s} = \varepsilon \\ &N_c^T = \sigma_s A_s \\ &\sigma_y^N = \sigma_s = \frac{N_c^T}{A_s} = \frac{N_c^T}{\pi(R^2 - (R-t)^2)} \approx \frac{N_c^T}{2\pi Rt} \end{aligned} \tag{16}$$

From the assumption of plane-section, the following equation is given

$$\sigma_s = E_s\varepsilon = E_s\frac{r\cos\theta}{\rho}(R - t \le r \le R) \tag{17}$$

where r = the distance between the stress unit and the center of the cross-section of circular column, E_s = modulus of elasticity of steel tube at the bottom panel zone, and ρ = radius of curvature of circular section bending.

From equilibrium conditions of the partition, the following equation is obtained

$$\begin{aligned} M_c^T &= 2\int_{R-t}^{R}\int_{-\pi/2}^{\pi/2} r\mathrm{d}\theta\cdot\mathrm{d}r\cdot\sigma_s\cdot r\cos\theta \\ &= \frac{E_s}{\rho}\frac{\pi}{4}\left[R^4 - (R-t)^4\right] \\ &= \frac{E_s}{\rho}I_z \end{aligned} \tag{18}$$

where I_z = moment of inertia of ring area to z axis.

Eq. (18) is given as follows

$$\frac{1}{\rho} = \frac{M_c^T}{E_s I_z} \tag{19}$$

Introducing Eq. (19) into Eq. (17), the following equation is obtained

$$\sigma_{\mathrm{s}}=\frac{M_{\mathrm{c}}^{\mathrm{T}}\cdot r\cos\theta}{I_{\mathrm{z}}},\qquad \sigma_{\mathrm{y}}^{\mathrm{M}}=\sigma_{\mathrm{s}}\Big|_{\substack{r=R\\ \theta=\pi}}=\frac{M_{\mathrm{c}}^{\mathrm{T}}\cdot R}{I_{\mathrm{z}}} \tag{20}$$

Introducing Eqs. (16) and (20) into Eq. (15), and designating $\sigma_x = 0.1f_y$, so the following equation is obtained

$$\tau_{\max}=\sqrt{\frac{f_{\mathrm{y}}^{2}-(0.1f_{\mathrm{y}})^{2}-(\frac{N_{\mathrm{c}}^{\mathrm{T}}}{A_{\mathrm{s}}}+\frac{M_{\mathrm{c}}^{\mathrm{T}}R}{I_{\mathrm{z}}}\cos\theta_{0})^{2}-0.1f_{\mathrm{y}}(\frac{N_{\mathrm{c}}^{\mathrm{T}}}{A_{\mathrm{s}}}+\frac{M_{\mathrm{c}}^{\mathrm{T}}R}{I_{\mathrm{z}}}\cos\theta_{0})}{3\sin^{2}\theta_{0}}} \tag{21}$$

When $\theta_0 = \pi/2$, Eq. (21) has an extreme value. The following equation is given

$$\begin{aligned}\tau_{\max}&=\sqrt{\frac{f_{\mathrm{y}}^{2}-(0.1f_{\mathrm{y}})^{2}-(\frac{N_{\mathrm{c}}^{\mathrm{T}}}{A_{\mathrm{s}}})^{2}-0.1f_{\mathrm{y}}\frac{N_{\mathrm{c}}^{\mathrm{T}}}{A_{\mathrm{s}}}}{3}}\\ &=f_{\mathrm{y}}\sqrt{\frac{1}{3}(0.99-n^{2}-0.1n)}\end{aligned} \tag{22}$$

where n is axial compression ratio of circular column, namely $n=\frac{N_c^T}{f_y A_s}$.

4.4 Calculation of shear capacity on Section B-B

Introducing Eq. (22) into Eq. (9), we have the formula of shear strength of the bottom panel zone

$$V_{\mathrm{vk}}^{\alpha}=\pi Rtf_{\mathrm{y}}\left[0.1\cot\alpha+\sqrt{\frac{1}{3}(0.99-n^{2}-0.1n)}\right] \tag{23}$$

When the horizontal shear strength of bottom panel zone has been calculated, the shear capacity of bottom panel zone can be calculated under horizontal force. Therefore, when α is equal to $\pi/2$, the following equation is the shear capacity of horizontal cross-section for SDC joints, including the effect of axial force on the shear capacity

$$V=\pi Rtf_{\mathrm{y}}\sqrt{\frac{1}{3}(0.99-n^{2}-0.1n)} \tag{24}$$

The shear capacity of joint was proposed in AISC (2005) as follows

$$V_{\mathrm{u}}=0.6f_{\mathrm{y}}d_{\mathrm{c}}t_{\mathrm{w}}(1+\frac{3b_{\mathrm{cf}}t_{\mathrm{cf}}^{\ 2}}{d_{\mathrm{b}}d_{\mathrm{c}}t_{\mathrm{w}}}) \tag{25}$$

where f_y = yield strength of steel at the panel zone; d_c = height of column section; t_w = thickness of web at the panel zone; b_{cf} = width of column flange; t_{cf} = thickness of column flange, and d_b = height of cross-section of lintel.

The second item in the bracket of Eq. (25) accounts for the contribution of circular column flanges to the shear capacity of bottom panel zone, the following equation is obtained

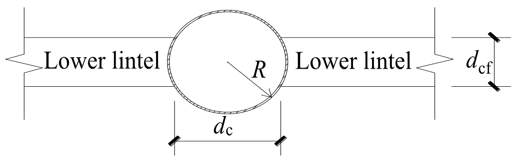

Fig. 17 Cross-section of panel zone

Table 4 Comparison of the shearing force between the test results and calculated values

Specimen No.	V_t /kN	V_e /kN	V_t / V_e	Mean value	Standard deviation
IJ-1	628.63	594.81	1.06	1.03	0.04
IJ-2	512.19	481.45	1.06		
EJ-1	578.12	594.81	0.97		
EJ-2	490.75	481.45	1.02		

$$V=\pi Rtf_{\mathrm{y}}\sqrt{\frac{1}{3}(0.99-n^{2}-0.1n)}(1+\frac{3b_{\mathrm{cf}}t_{\mathrm{cf}}^{\ 2}}{d_{\mathrm{b}}d_{\mathrm{c}}t_{\mathrm{w}}}) \tag{26}$$

In order to simplify the calculation, the shape of the panel zone is assumed to a rectangle in Fig. 17. The specimens in this test were designed by Construction Methods of Song dynasty (Li 1100), and the sizes of lintels and columns were determined by class material of timber in song dynasty, where d_b = 27 parts; R = 21 parts; b_{cf} = 18 parts; d_c = 36 parts, in which 'part' is a length unit in Construction Methods of Song dynasty (Li 1100), and the subscript's' indicates the second-class material of timber, and designating $t_w = 2t$, and $t_{cf} = t$. Therefore, the Eq. (26) is simplified as follows

$$V=\pi Rtf_{\mathrm{y}}\sqrt{\frac{1}{3}(0.99-n^{2}-0.1n)}(1+\frac{7t}{12R}) \tag{27}$$

Based on the experimental and theoretical analysis of SDC joints, Eq. (27) is derived in which the second item in the last bracket accounts for the contribution of circular column flanges to the shear capacity of bottom panel zone. It is worth noting that Eq. (27) is only applicable to the SDC joints and the axial compression ratio of the joints is less than 0.6.

Table 4 shows the comparison of the shear capacity between the test results and calculated values, where V_t = yield shearing force in tests calculated by Eqs. (2)-(3) (Eqs. (5)-(6)); V_e = yield shearing force calculated by Eq. (27). The results show that the mean value and standard deviation of V_t/V_e are 1.03 and 0.04, respectively. It is shown that the calculated values show good agreement with the test results.

5. Bending capacity verification at middle panel zone

From the failure modes and force characteristics of middle panel zone for IJ series, the bending bearing

Table 5 Bending capacity at middle panel zone

Specimen No.	Load stage	n^*	$\frac{N_c^T}{A_s}$ /MPa	$\frac{M_c^T}{W_s}$ /MPa	σ_{max} /MPa
IJ-1	P_y	0.3	65.18	207.95	273.13
	P_u	0.3	65.18	266.09	331.26
	P_m	0.3	65.18	226.18	291.36
IJ-2	P_y	0.6	130.36	188.24	318.60
	P_u	0.6	130.36	244.29	374.64
	P_m	0.6	130.36	208.48	338.84
EJ-1	P_y	0.3	65.18	149.13	214.31
	P_u	0.3	65.18	203.27	268.44
	P_m	0.3	65.18	172.77	237.95
EJ-2	P_y	0.6	130.36	165.55	295.91
	P_u	0.6	130.36	198.55	328.91
	P_m	0.6	130.36	151.57	281.93

$^*n$: Axial compression ratio of the panel zone of circular column

capacity of the middle panel zone shall be checked by the equation as follows

$$\sigma_{max} = \frac{N_c^T}{A_s} + \frac{M_c^T}{W_s} \tag{28}$$

where A_s = cross-section area of circular column at the middle panel zone; W_s = section modulus in bending, and σ_{max} = maximum normal stress of cross-section of circular column at the middle panel zone; N_c^T = axial force of circular column-end at middle panel zone; M_c^T = bending moment of circular column-end at middle panel zone.

When the specimens reached ultimate bearing capacity, the values (except EJ-1) of σ_{max} listed in Table 5 was more than the yield strength of steel tube in 6mm thickness, and local buckling formed on both sides of middle panel zone (except EJ-1). It is illustrated that the steel on sides of middle panel zone had yielded, which had good agreements with the calculated values.

6. Conclusions

The following conclusions can be drawn based on the experimental and theoretical analyses of four 1/2-scaled SDC joints presented in this paper:

- The typical failure modes of SDC joints in Chinese traditional style buildings are shear buckling at bottom panel zone, bending failure at middle panel zone, welds fracturing at panel zone, as well as tension failure of base metal in the heat-affected zone of panel zone.
- The experimental and theoretical study results indicate that SDC joints had good seismic performance and energy dissipation capacity. The bearing capacities of IJ series were higher than those of EJ series with the same axial compression ratio. And also, the ultimate loads of the specimens with axial compression ratio 0.3 were higher than those of the specimens with axial load level 0.6.
- To provide a theoretical basis for the shear design of SDC joints under horizontal seismic loading, the shear capacity equation of bottom panel zone for the joints is proposed, based on the stress state of random element at the bottom panel zone.
- In order to avoid that the failure occurs at the middle panel zone of SDC joints, the bending capacity of the middle panel zone was checked besides the calculation of the shearing capacity at the bottom panel zone.

Acknowledgments

The authors would like to thank National Natural Science Foundation of China (Grant No. 51678478), National “Twelfth Five-Year” Plan for Science & Technology of China (Grant No. 2014BAL06B03), Shaanxi Science and Technology Research and Development Projects (Grant No. 2013KW23-01) and Xi’an University of Architecture & Technology for their generous support of this research work.

References

AISC (2005), Load and resistance factor design specification for structural steel buildings; American Institute of Steel Construction, Chicago, IL, USA.

Chen, C.C. and Lin, C.C. (2013), “Seismic performance of steel beam-to-column moment connections with tapered beam flanges”, *Eng. Struct.*, **48**, 588-601.

D’Ayala, D. and Benzoni, G. (2012), “Historic and traditional structures during the 2010 Chile earthquake: observations, codes, and conservation strategies”, *Earthq. Spectra*, **28**(S1), S425-S451.

Gholami, M., Deylami, A. and Tehranizadeh, M. (2013), “Seismic performance of flange plate joints between steel beams and box columns”, *J. Constr. Steel Res.*, **84**, 36-48.

Hiroki, N., Atsushi, S. and Keiichiro, S. (2011), “Loading Test of Exterior Diaphragm Type Moment Connection with Circular Tube Column”, *Steel Constr. Eng.*, **18**(72), 53-60.

Kim, Y.P. and Hwang, W.S. (2008), “Evaluation of diaphragm effect for steel welded box beam and circular column connections”, *Int. J. Steel Struct.*, **8**(3), 189-198.

Kim, J., Hong, W.K. and Kim, J.H. (2016), “Experimental investigation of the influence of steel joints upon the flexural capacity of precast concrete columns”, *Struct. Des. Tall Special Build.*, **26**(5), e1340.

Lan, X.Y. and Huang, Y. (2016), “Structural design of cold-formed stainless steel tubular X-and T-joints at elevated temperatures”, *Thin-Wall. Struct.*, **108**, 270-279.

Lee, K.M., Li, R., Jung, H.T., Chen, L.Y. and Oh, K.W. (2013), “Cyclic testing of weak-axis steel moment connections”, *Steel Compos. Struct., Int. J.*, **15**(5), 507-518.

Li, J. (1100), *Construction Methods of Song Dynasty*, Royal Press, Kaifeng, China.

Liang, S.C. (1984), *A Pictorial History of Chinese Architecture*, MTT Press, Boston, MA, USA.

Loulelis, D., Hatzigeorgiou, G.D. and Beskos, D.E. (2012), "Moment resisting steel frames under repeated earthquakes", *Earthq. Struct., Int. J.*, **3**(3), 231-248.

Moradi, S. and Alam, M.S. (2017), "Multi-criteria optimization of lateral load-drift response of posttensioned steel beam-column connections", *Eng. Struct.*, **130**, 180-197.

Shi, G., Fan, H., Bai, Y., Yuan, F., Shi, Y.J. and Wang, Y.Q. (2012), "Improved measure of beam-to-column joint rotation in steel frames", *J. Constr. Steel Res.*, **70**, 298-307.

Wang, W. Chen, Y.Y., Li, W.Q. and Leon, R.T. (2011), "Bidirectional seismic performance of steel beam to circular tubular column connections with outer diaphragm", *Earthq. Eng. Struct. Dyn.*, **40**(10), 1063-1081.

Xue, J.Y. and Qi, L.J. (2016), "Experimental studies on steel frame structures of traditional-style buildings", *Steel Compos. Struct., Int. J.*, **22**(2), 235-255.

Zhang, X.C., Xue, J.Y., Zhao, H.T. and Sui, Y. (2011), "Experimental study on Chinese ancient timber frame building by shaking table test", *Struct. Eng. Mech., Int. J.*, **40**(4), 453-469.

CC